Modelling and Measurement of Diffraction Patterns to Characterize Next-Generation Optical Systems in CMB Cosmology

Alec T. Josaitis
University of Michigan – Ann Arbor
December 12th, 2017

A thesis submitted to the Department of Physics, University of Michigan, in partial fulfillment of the requirements for the degree of Bachelor of Science with an Honors Concentration in Physics. This thesis represents my own work in accordance with University regulations.

1. Introduction

Since antiquity, man has sought to understand the origin of the Universe; the field of cosmology seeks to resolve this mystery in a scientifically-consistent manner. The cosmic microwave background (CMB), relic thermal radiation released in the early universe which is now the oldest observable light in the universe, provides unparalleled support for the Hot Big Bang theory, which predicts the state of the universe until the first 10^{-32} seconds after its inception. Many scientific instruments have been, and continue to be, built to more precisely measure the properties of the CMB; effectively all of these instruments require diffraction-limited optical systems. This level of optical resolution requires careful characterization of the diffraction patterns caused by all optical elements in a telescope system. This thesis motivates and describes an ongoing experiment to characterize the diffraction patterns of an optical system used by the Atacama Cosmology Telescope (ACT) collaboration, and presents a holographic imaging technique which may be used to measure amplitude and phase modulations of diffraction patterns found in next-generation instrumentation for CMB cosmology.

1.1 An Historical Primer to CMB Isotropy and Homogeneity

The CMB is the oldest observable light in the universe. These relic photons have been free-streaming, largely unperturbed, through the universe since the time of last scattering, which occurred approximately 380,000 years after the Big Bang [1]. Since the photons have been largely unperturbed, they serve as a powerful tool to study the homogeneity and isotropy of the early universe. If the universe contained no fluctuations in density over its entire volume, and expanded isotropically until the time of last scattering, we would expect the CMB at the time of last scattering to be a perfect blackbody. As such, the temperature of the CMB would be

purely isotropic; the temperature of the CMB would never deviate from its mean value. Since 1965, we have had observational evidence that the CMB can be, to several orders of magnitude, modelled by a blackbody spectrum.

On May 7th, 1965, four faculty of the Princeton Physics department (R.H. Dicke, P.J.E. Peebles, P.G. Roll, and D. T. Wilkinson), offered theoretical explanations for why the relic "fireball" of radiation leftover from the big bang would appear as thermal radiation with a blackbody spectrum [3]. Six days later on May 13th, 1965, the first observational evidence of this relic cosmic radiation came largely by accident from A. A. Penzias and R.W. Wilson, who were trying in vain to explain an excess microwave signal coming from a horn antenna they operated at Bell Telephone Laboratories in Homdel, New Jersey. According to Penizas and Wilson, "The excess temperature [3.5 ± 1 K] is, within the limits of our observations, isotropic, unpolarized, and free from seasonal variations", and that their complete analysis of known terrestrial and atmospheric signals "...clearly eliminate[s] the possibility that the radiation [they] observe[d] is due to radio sources of types known to exist" [4]. After decades of follow-up studies, we now know that Penzias and Wilson measured the CMB (a definitive measurement was given by WMAP at 2.726 K) and offered the first observational proof that the universe was in thermal equilibrium at the time of last scattering. Knowing this, cosmologists may rightfully apply well-understood laws of thermodynamics (such as the modelling of thermal radiation by a blackbody spectrum) to the study of the evolution of the early universe. However, any form of anisotropic expansion of the Universe, or fluctuations in the density of the universe, would be encoded as temperature anisotropies in the CMB at the time of last scattering and could not be modelled by classical thermodynamics [2].

1.2 CMB Temperature Anisotropies

Having confirmed that the CMB is, to a large degree, isotropic, current studies of the CMB determine how and to what degree the CMB is anisotropic. Knowing that the anisotropy is small compared to the blackbody behaviour of the CMB, one natural modelling of the anisotropy is as noise – via a Gaussian random field of unit variance. For noise-like phenomena, we are interested in the amplitude of anisotropies as a function of scale. Physically, we wish to study the angles through which CMB power is subtended on the present-day sky. Since the CMB field is defined on the surface of a sphere, we must solve Laplace's equation to study the angular decomposition of CMB anisotropy:

$$\nabla^2 \psi = 0$$

$$\psi(\theta, \phi) = \Theta(\theta)\Phi(\phi) = 0$$

$$\frac{\Phi(\phi)}{sin\theta}\frac{d}{d\theta}\left(\sin\theta \frac{\mathrm{d}\Theta(\theta)}{d\theta}\right) + \frac{\Theta(\theta)}{sin^2\theta}\frac{d^2\Phi(\phi)}{d\phi^2} + l(l+1)\Theta(\theta)\Phi(\phi) = 0$$

the solution to this equation on a sphere are the spherical harmonic functions [5]:

$$\psi = \sqrt{\frac{2l+1(l-m)!}{4\pi(l+m)!}} P_{lm}(cos\theta)e^{im\phi} \equiv Y_{lm}(\theta,\phi)$$

for $l \geq 0$ and $m = -l,\ldots,l$. where the spherical harmonics are, in effect, normalized Legendre polynomials, P_l:

$$Y_l^m(\theta,\varphi) = Ne^{im\varphi}P_l^m(cos\theta)$$

where N is a normalization constant. It is useful to note that the multipole moment, *l*, is related to the angle subtended on the sky by the following, simple, relation [6]:

$$\frac{180}{\theta} \sim l$$

An angular power spectrum decomposition of the CMB allows one to study the amplitude squared of the magnitude of CMB temperature fluctuations as a function of the angle subtended on the CMB sky. Experimentally, we must analyze in pairs of directions, $\hat{n}$ and $\hat{n}'$, that are separated by an angle θ so that $\hat{n} \cdot \hat{n}' = cos\theta$. Averaging over all such pairs, we obtain a two-point correlation function, $C(\theta)$ [6].

$$< dT(\hat{n})dT(\hat{n}') > \equiv C(\theta) = \sum_l \frac{(2l+1)}{4\pi} C_l P_l(cos\theta)$$

Using the flat-sky approximation, an analysis of the CMB anisotropies may be further simplified into a series of operations to be performed on a 2x2 matrix of sky data [7]. Multipole moments, *l*, are directly related to the conventional k-modes of a 2D discrete Fourier transform. Indeed, l can be interpreted as a radial Fourier mode [7]:

$$l = 2\pi k = 2\pi\sqrt{k_x^2 + k_y^2}$$

Thus, under the assumption that the universe is isotropic (no x-direction is preferred to any y-direction, and vice versa), we can model two degrees of anisotropy, *x* and *y*, with one variable, l. Further, according to the convolution theorem, a convolution (*) in the time-domain, where us cosmologists observe the universe, is equivalent to multiplication (·) in the frequency domain, the space occupied by the output of a CAMB simulation. Specifically [5],

$$F^{-1}\{F[A] \cdot F[B]\} = A * B$$

Using this relation, we may model CMB temperature anisotropies as a convolution of a Gaussian random field across our angular power spectrum, C_l.

Let us now use this theoretical understanding of temperature anisotropies to analyze an ideal simulation of the CMB power spectrum. The data used in this analysis was generated by inputting standard ΛCDM parameters into A. Lewis and A. Challinor's Code for Anisotropies in the Microwave Background (CAMB). I used an iPython notebook to structure my analysis, program functions in Python, and observe the analysis through a convenient web-based interface. Much of the code used for my analysis was written by J. J. McMahon and R. Hlozek for their 2016 Summer School on CMB Data Analysis [7]. Exercises were left for summer school students to complete individually; solutions to these exercises motivate much of my analysis.

A CAMB simulation outputs power spectrum components, D_l, which are related to the

standard angular power spectrum moments, C_l, by the following expression [7]:

$$D_l = \frac{l(l+1)}{2\pi} C_l$$

Using this conversion, one may use the convolution theorem to graphically represent the calculation of a CMB temperature map:

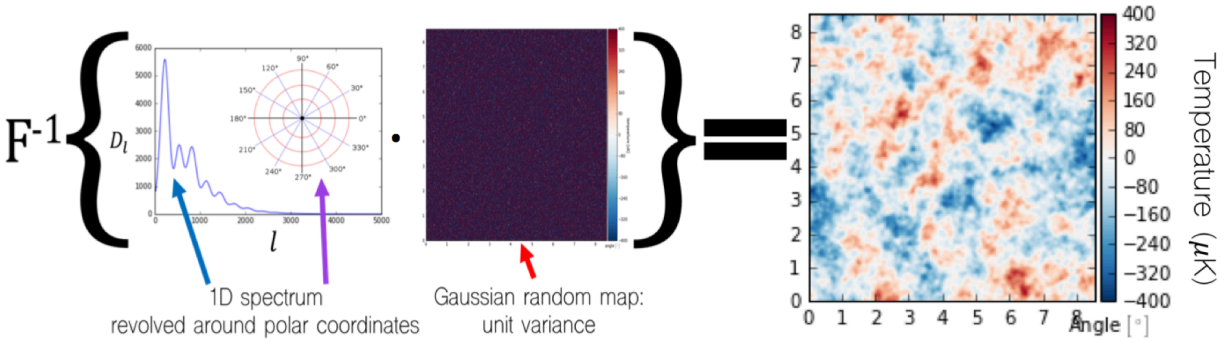

FIGURE 1. A graphic illustration of how the convolution theorem is used to create a 2D temperature anisotropy map of the CMB from a 1D angular power spectrum. The angular power spectrum used here was generated by a CAMB simulation using standard ΛCDM parameters.

In Figure 1, we observe that the most common width of temperature anisotropy features is ~1 degree, which corresponds to a multipole value of $l\sim$ 180. This is expected, as I input into CAMB the conventional ΛCDM parameters, which produce a spatially flat universe. Lastly, we observe from the y-axis of the temperature map that the anisotropy of the CMB manifests itself on the order of μK, which is 1 part in 10^4 of the observed CMB temperature of ~2.7K. Thus, using a CAMB simulation of a conventional ΛCDM universe, we rightly conclude that our universe is spatially flat and that the CMB is isotropic to 1 part in 10^4.

1.3 Analyzing CMB Data from the Atacama Cosmology Telescope

What would happen if we took raw data from a CMB experiment and, using the same data analysis method, plotted a 2D map of temperature anisotropy? Well, let's try that, and compare this map (Fig. 2) to an idealized CMB simulation (Fig. 1), and convince ourselves that experimental data contains distinct features that are not found in an idealized CMB simulation. The experimental data I used is public, published data from the ACT's third season, taken at 148 GHz [8].

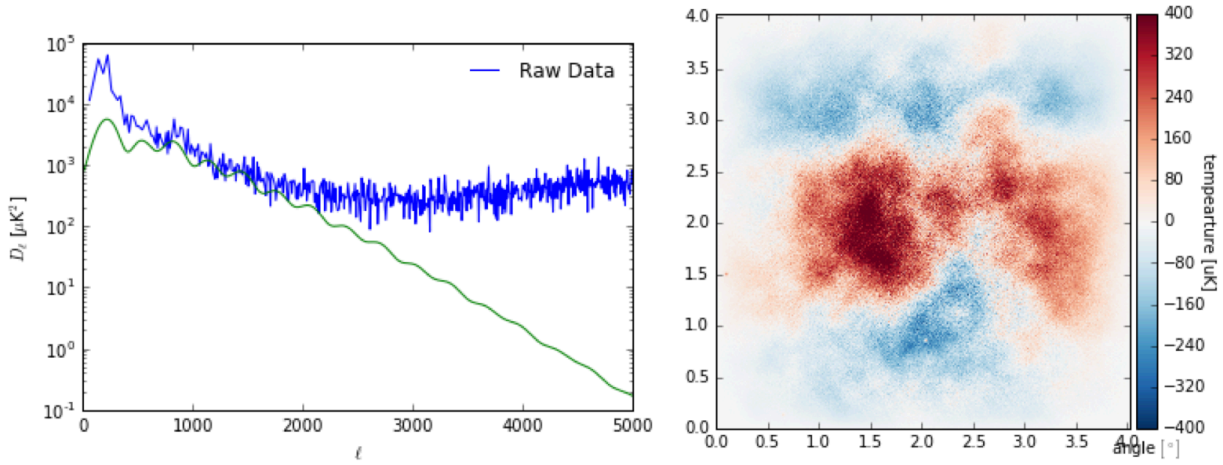

FIGURE 2. Power spectrum and temperature anisotropy map of raw, public, ACT season 3, 148GHz data. The power spectrum of the raw experimental data (blue) is compared to a CAMB-simulated ΛCDM universe.

It is clear to see that the power spectrum and temperature map of the raw experimental data deviate significantly from their CAMB-simulated counterparts. To understand why, we must first acknowledge that we are no longer observing *solely* the CMB - An absentminded undergraduate may have touched a telescope component and caused more noise in your signal, the sky you are observing contains point sources (stars and galaxies, for example), light travelling through your telescope's optical system may be diffracting, etc.; all of these factors will nontrivially affect your CMB temperature map. Let us briefly discuss various effects which contaminate raw CMB data and how to subtract these extraneous features from your data in order to view, to the best of your ability, *only* the features of the CMB.

1.4 Point Sources and SZ Signals

In a CMB map, point sources (such as galaxies) appear as frequency-dependent dots of temperature which vary significantly from the mean temperature of a CMB map. Three types of point sources which most heavily contaminate a CMB map are active galactic nuclei (AGN), dusty star-forming galaxies (DSFG), and the imprints of galaxy clusters due to the Sunyaev-Zel'Dovich (SZ) Effect [7]. AGN and DSFG can be naively modelled as a randomly-distributed combination of sources of fixed peak brightness. Following the recommendations of Hlozek and McMahon, I chose to model, over a 10x10 degree patch of sky, AGN and DSFG as a combination of both 5000 point sources with a peak brightness of $\sim 10\ \mu K$ with a Poisson distribution of brightness, and also 500 sources with a peak brightness of $\sim 100\ \mu K$ with a wider, exponential brightness distribution. The values of 500 and 5000 points sources were

not arbitrary; they are order-of-magnitude approximations to the number of point sources found in an actual 10x10 degree patch of sky at 150 GHz [7].

To account for SZ signals, whose brightness on a CMB temperature map are inherently a function of the frequency of the CMB one is measuring, a "beta" profile of peak point-source brightness was used [7]. Note that this is different than the model used for AGN and DSFG, where the peak brightness remains fixed and different brightness distributions are used around the peak. To simplify my model of SZ signals, I only varied signal brightness, and left all SZ signals to have the same angular diameter and exponential distribution of brightness away from the peak. A more robust analysis would include SZ signals of varying angular diameters and brightness distributions. Fig. 3 is my simulation of point sources and SZ signals on a 10x10 degree patch of sky.

1.5 Instrumental Effects, Atmospheric Noise, and Diffraction-Limited Optical Systems

Any instrument designed to measure the CMB (whether ground based, like the ACT, or space-based, such as the Planck Satellite) carries with it its own set of noise and limitations. Several of these features have direct impacts on a CMB power spectrum (and thus, a temperature anisotropy map) produced by these instruments which must be accounted for. Below we will observe the effects of 1/f noise, diffraction from the main beam inside a CMB optical system, instrumental effects, and atmospheric noise.

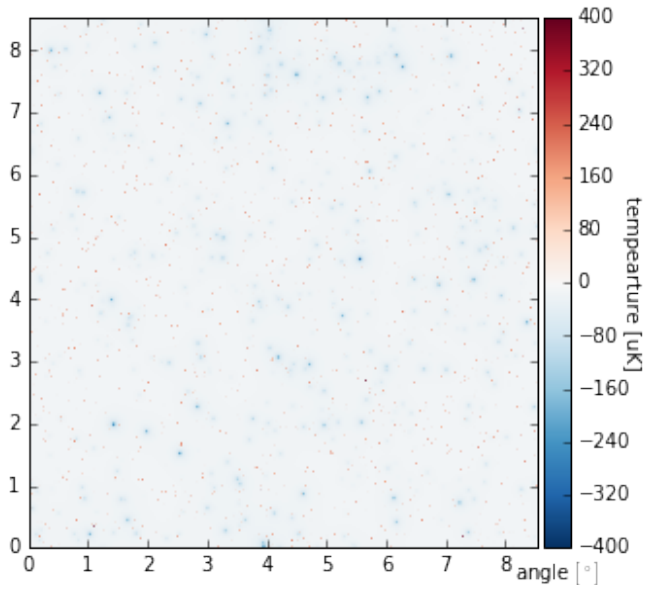

FIGURE 3. Simulated point sources and SZ clusters for a 2D CMB temperature map.

The electronics of any detector in a CMB instrument will suffer from a characteristic 1/f noise, which tends to leave large stripes running across the patch of sky observed by your instrument, such as those running horizontally across Figure 4. The direction of the striping is a direct result of the direction across which an instrument (such as a telescope) swept a patch of sky [7]. Thus, instruments with complex "scanning patterns" will suffer from complex, but repeatable and distinct, striping patterns [7].

Ground-based CMB telescopes, such as the ACT, suffer from another distinct and significant type of noise, which is that caused by atmospheric turbulence. The peak power of

turbulence subtends a large angle on the sky (~1 degree), and so the effect of turbulence is to over-estimate the power coming from the first peak of a CMB power spectrum. This can easily be observed in Figure 2.

The optical systems of any CMB instrument have finite resolution, meaning a beam of CMB photons has a finite width as it propagates through the lenses, filters, and/or mirrors of a CMB instrument. Consequently, any instrument measuring the CMB suffers from the effects of diffraction [7]. One can observe the effects of beam diffraction by modelling the beam as a 2D Gaussian function and convolving it with a temperature map of the CMB. I will now demonstrate this graphically.

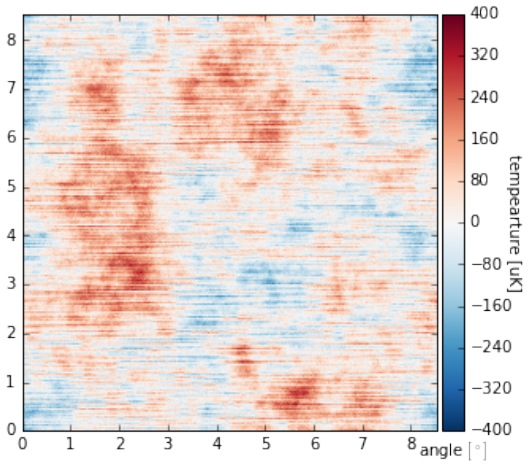

FIGURE 4. 1/f detector noise causes distinct, "striped" features across a 2D CMB temperature map. In an actual experiment, the direction of the striping is related to direction across which a telescope scanned a particular patch of sky, which can yield a more complex pattern that the horizontal one produce above.

Beam diffraction blurs the features of a CMB temperature anisotropy measurement. The amount of blurriness depends on the width of your beam, with smaller beams suffering less from diffraction. CMB optical systems have three characteristic beam widths [7]. Large angular scale B-mode observatories, such as Spider, have ~10-50 arcminute beams [9]. Medium scale observatories, such as the High Frequency Instrument (HFI) of the Planck satellite, have ~3 arcminute beams [10]. High resolution observatories such as the ACT have ~1 arcminute beams [11]. Thus, an ACT map suffers less from beam effects than the Planck Satellite which suffers less than Spider. Beam diffraction is one example of a tradeoff between the "resolution" of your telescope compared with what fractional area of the CMB you would like to measure. To achieve their science goals, most CMB experiments require "diffraction-limited" optical systems, meaning that their data can be cleaned of all systematic effects to at least the resolution of beam diffraction, so that the only relevant limit to data resolution is the diffraction caused by optical system beam widths.

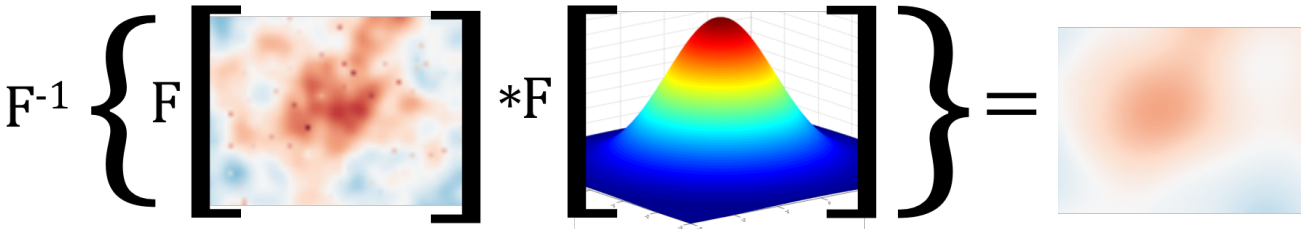

FIGURE 5. The effects of beam diffraction on a map of CMB temperature anisotropy. Since the beam of photons traveling in the optical system of an instrument has finite width (i.e. is not infinitely thin), the beam itself will blur features of your map, such as point sources and CMB temperature fluctuation.

1.6 Little Buddies and the Millimeter Bolometer Array Camera (MBAC)

CMB optical systems are often calibrated by creating temperature maps around well-characterized point source, such as a planet. Suppose that, after removing the point source from your temperature map, accounting for all known instrumental and systematic effects, and subtracting the effects of atmospheric noise, your temperature maps still contain unexpected features. If this is the case, your optical system may be seriously misbehaving, which would prohibit the system from achieving its intended diffraction-limited design constraints. Below is a point-source-calibration temperature map taken in the summer of 2016 with the Millimeter Bolometer Array Camera (MBAC), an ACT receiver. The MBAC includes three bolometer arrays operating at 148 GHz, 215 GHz, and 277 [11]; this photo is from the 215 GHz array. The unexpected features were later dubbed "Little Buddies".

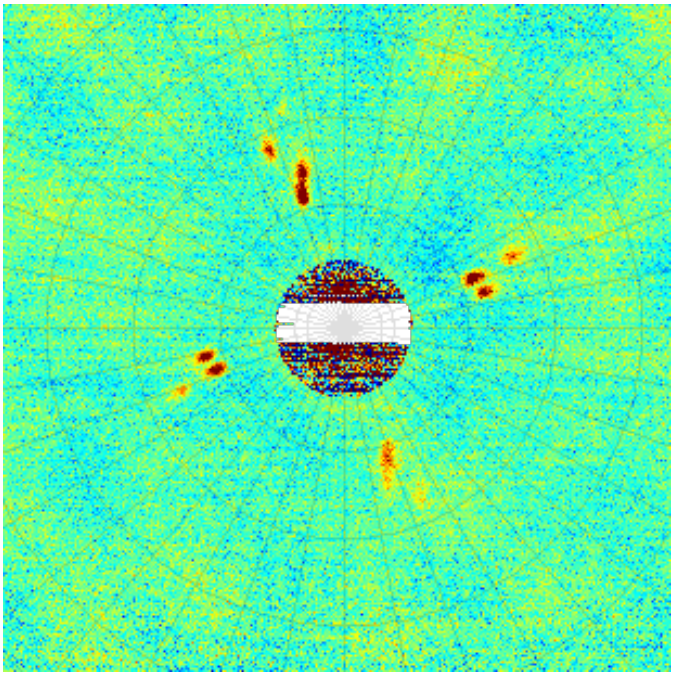

FIGURE 6. "Little Buddies" in a 20x20 deg. patch of sky around Saturn. The measurement was taken with the MBAC in the summer of 2016 and temperature fluctuations from the mean are here presented in linear scale. Red represents the largest positive (hot) deviation in temperature from the mean, blue represents the largest negative (cold) deviation from the mean, and green represent the mean temperature. Since this image is intended to only be a qualitative, not quantitative representation of the Little Buddies, a mK temperature scale is not included. The temperature of real CMB anisotropies can be observed as diffuse patches of blue, green, and yellow. The little buddies are twelve red spots in a near-symmetric, cross-like pattern around Saturn. The multi-color circle in the center of the photo does not represent temperature data, and is the remnants of masking Saturn out of the data. Courtesy of Sigurd Naess.

At the time of this measurement, it was expected that these twelve Little Buddies -

which form a near-symmetric, cross-like pattern around bright point sources– were caused by an unexpected diffraction pattern in the MBAC, though the source of the diffraction was not known. Eventually, it was suspected that a low-pass filter kept cryogenically cooled to 1K, placed at the Lyot stop of the MBAC arrays, is what was causing the Little Buddies (See Figure 8 for location of this filter in the MBAC). To confirm this, I was tasked to recreate the Little Buddies in the laboratory. My studies of diffraction patterns caused by the 1K low-pass filter are discussed below.

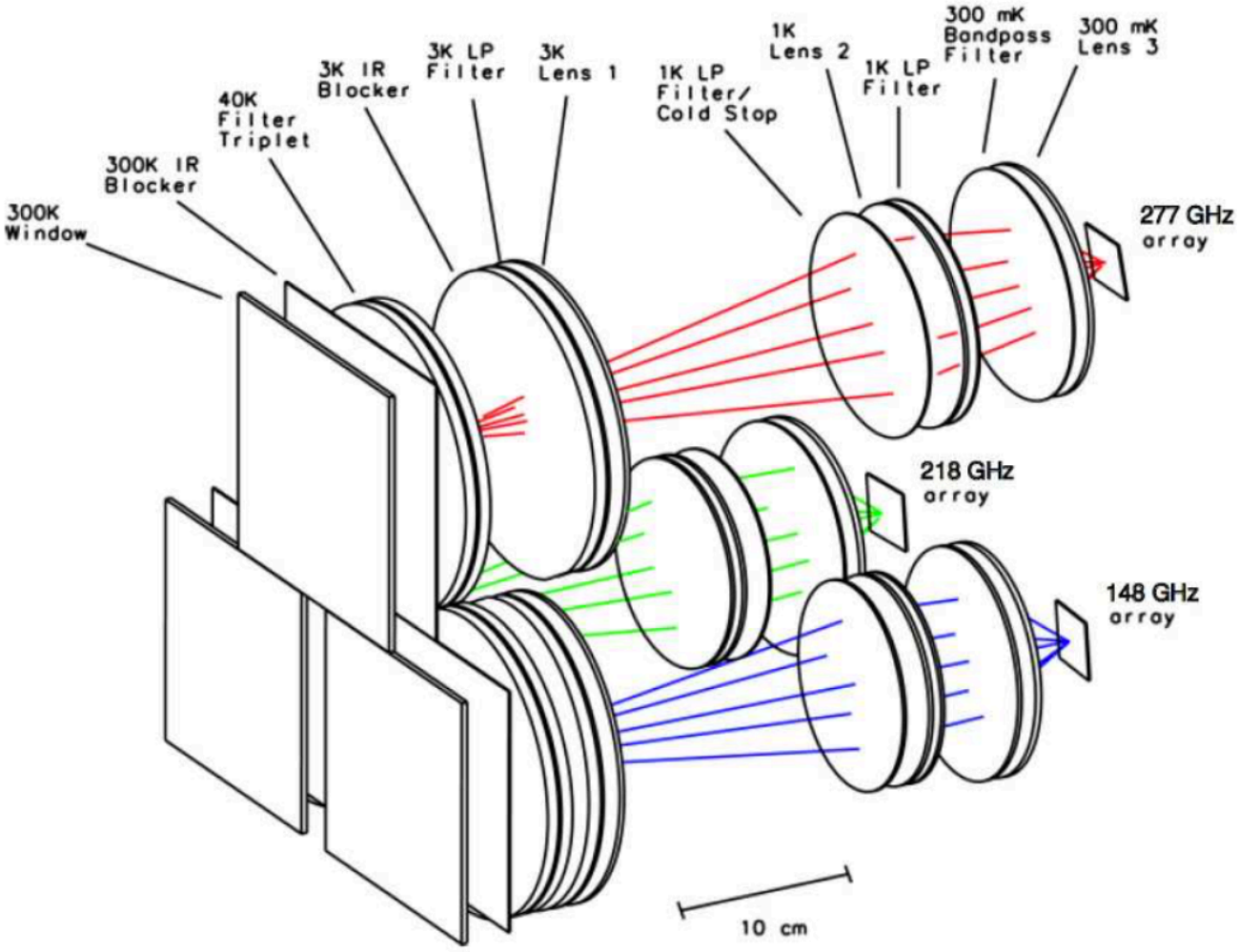

FIGURE 7. Three dimensional model of the cold reimaging optics for MBAC. The optical elements for each array are separated into individual optics tubes. Each array has a similar set of optical elements. The 277 GHz elements and temperatures are labeled. The lenses are labeled Lens 1 to 3, with Lens 1 one being closest to the 300 K window. The low-pass capacitive-mesh filters are labeled LP and the band-pass filter as BP. Infrared blocking filters are labeled IR. The temperature of the components decreases moving toward the arrays to reduce the loading, with the band-pass filter, the third lens, and arrays all held at 0.3 K [12].

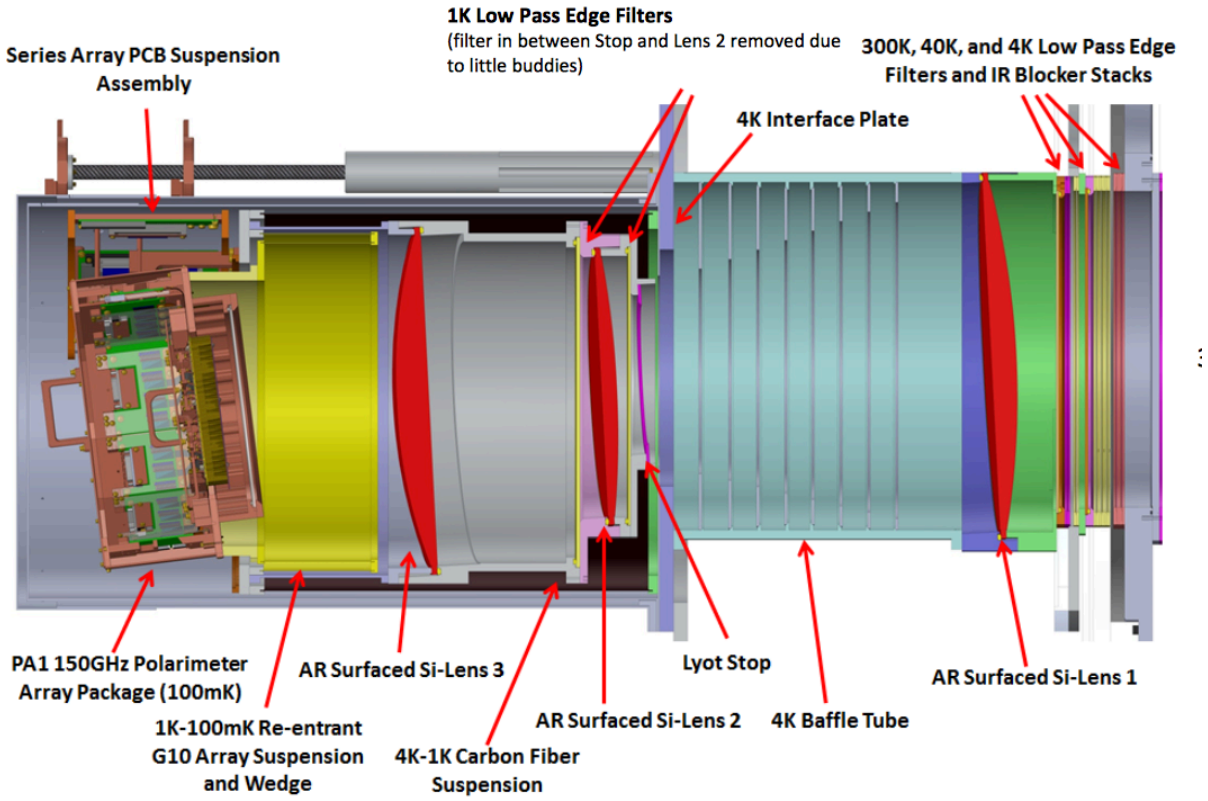

FIGURE 8. A cross-sectional view of the MBAC's 215 GHz Array. The 1K low pass filter was situated next to the Lyot stop, but was removed by the time this figure was made, due to the concern over Little Buddy diffraction patterns.

2. Amplitude Modulation Beam Mapping

2.1 Science Goals

We seek to qualitatively, but not quantitatively, determine whether the 1K low-pass filter found at the Lyot Stop of the MBAC is the source of the little buddies found in Figure 6. To achieve this goal, a beam mapping setup was used to measure the spatial variation of beam intensity both with and without the MBAC filter.

2.2 Beam Mapping Setup

Figures 9-11 show the setup of the 2D beam mapping system used to measure the spatial variation of the MBAC filter. A Virginia Diodes (VDI) WR9.0 modular amplifier and multiplying chain produces a microwave signal of a single frequency, which falls within the range of frequencies detected by the MBAC 215 GHz array. This signal, a 2D Gaussian beam, is focused onto the receiver (Rx) horn using a plano-convex lens. Depending on what you are trying to measure, the MBAC filter can be firmly attached or removed from the front of the lens enclosure using microwave-transmissive Kapton tape. It is important to note that the MBAC filter is larger than the plano-convex lens. Thus, in order to measure the spatial variance of the diffraction patterns caused by the MBAC, we consider the filter to

have four quadrants: NW, NE, SW, and SE. Depending on which quadrant of the filter you would like to measure, portions of the other quadrants of the filter will hang-off the edge of the lens enclosure, and thus these portions will not be measured by the Rx Horn. In our experimental setup, only one quadrant can be fully measured by the Rx horn in any given 2D map, but during every 2D map we ensure that some portion of the MBAC filter fully covers the lens.

The Rx horn sits at the back of the lens enclosure, and is electrically isolated from the rest of the experimental setup (using electrically-isolating Nylon screws and Kapton tape) so as to avoid ground-loop effects with the Tx horn. The amplitude of the Rx signal is recorded. The Tx and Rx horn outputs are both covered with Kapton tape to assure that foreign materials do not enter the horns and affect their behavior.

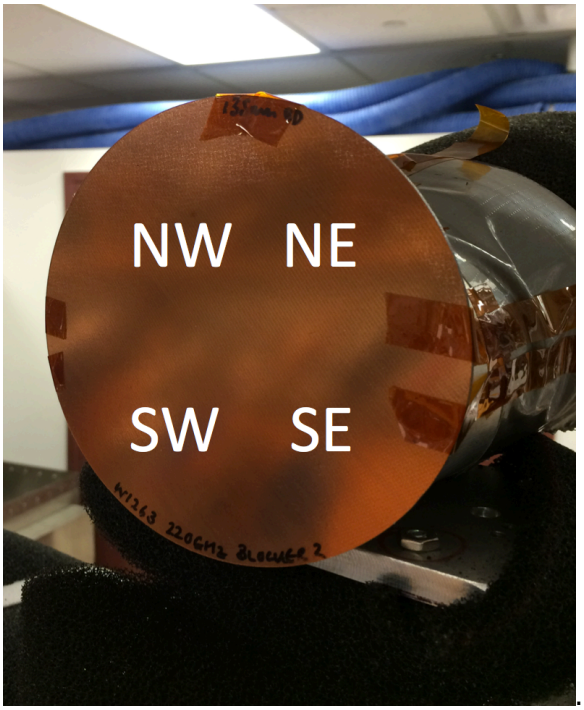

FIGURE 9. The MBAC 1K, low-pass filter is firmly attached to the outside of a plano-convex lens using microwave-transmissive Kapton tape. Since the filter is larger than the planar surface of the lens, we experimentally consider the filter to have four quadrants, all of which are individually tested.

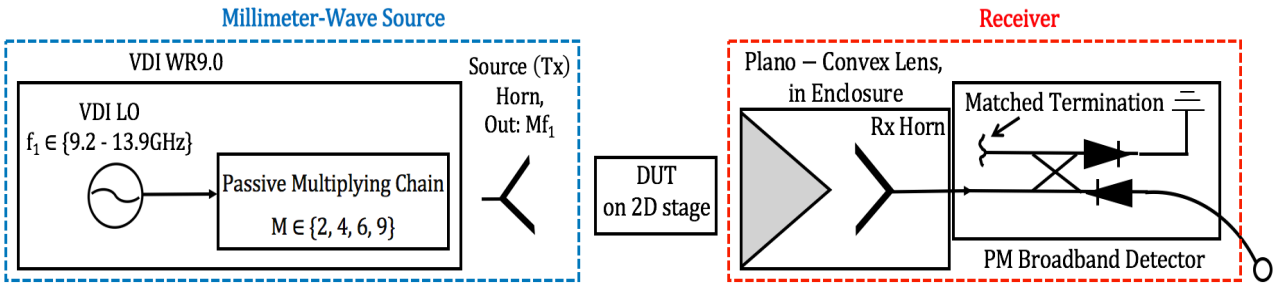

FIGURE 10. A millimeter-wave source radiates a 2D Gaussian beam onto an optical element which is to be tested (the "DUT"). The amplitude of the source signal is modulated by the DUT and the resulting amplitude is received by a feed horn and passed to a Pacific Millimeter broadband detector.

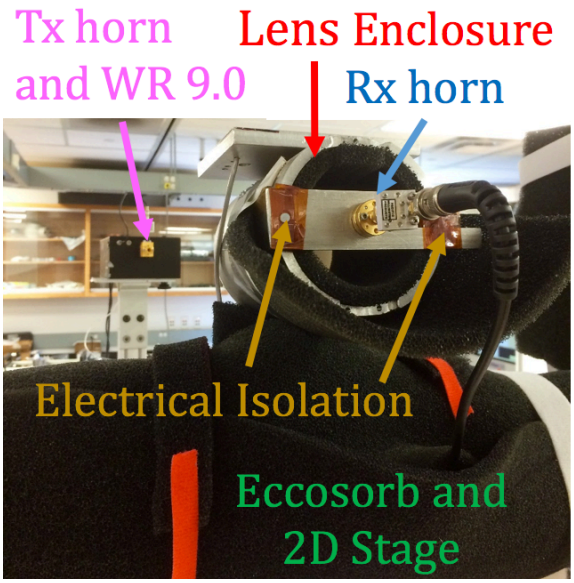

FIGURE 11. An image of the actual experimental setup. In the background, the Tx (source) horn is attached to a Virginia Diodes (VDI) WR9.0, which contains both the LO and a passive multiplying chain of the millimeter-wave source. In the foreground, a receiver (Rx) horn is electrically isolated from the rest of the setup, including the 2D beam stage. A Pacific Millimeter broadband detector outputs the Rx horn signal to a BNC cable. Eccosorb is placed on the 2D beam stage and plano-convex lens enclosure in order to avoid stray reflections into both the Tx and Rx horns.

While the Tx horn remains fixed throughout the entire experiment, the Rx horn and lens enclosure are mounted to a 2D beam mapping stage which can rotate in azimuth and elevation. Each rotational degree of freedom is powered by a separate Velmex rotary table, which have a repeatable rotational accuracy of $1/80^{th}$ of one degree. A high-loss microwave absorbing material, called Eccosorb, is placed inside the lens enclosure and around most of the 2D beam mapping stage in order to avoid stray reflections from entering either the Tx or Rx horns. The entire experimental setup (WR 9.0, Tx and Rx horns, and lens enclosure) are placed in the center of as large of a room as possible, so that spurious microwave signals from the laboratory environment are least-likely to free-stream or reflect into our experimental setup.

2.3 Procedure

The passive multiplying chain of the WR9.0 is setup such that the millimeter-wave source radiates a 200 GHz, 2D Gaussian beam out of the Tx horn. With this signal being output, a 20x20 degree beam map (in azimuth and elevation) is created (*without the MBAC filter*) by recording the amplitude of the Rx signal at every half-degree step of the Velmex motors. Thus, there are 1600 measurements in this dataset. The MBAC filter is then rigidly attached to the exterior of the plano-convex lens using Kapton tape; it is attached in such a way that one quadrant of the filter will be fully measured, and that all of the lens is covered by the filter. With the filter attached, another 2D beam map of the same 1600 angular steps is measured. This beam mapping process is repeated for the other three quadrants. Then, the filter is removed and another no-filter beam map is created.

After all of the beam maps are created, we calculate the peak-normalized difference of

each of the four quadrants with respect to the no-filter measurement. We also record a second no-filter measurement and its peak-normalized difference to the first no-filter measurement. This no-filter peak-normalized difference is used to determine the degree of repeatability offered by our experiment.

2.4 Results

The results of our experiment are given in Figures 12 and 13. The data in each figure is from the same 200 GHz dataset. The only difference between the two figures is that the peak-normalized differences in Figure 12 are plotted in linear scale and the same differences are plotted in dB scale in Figure 13.

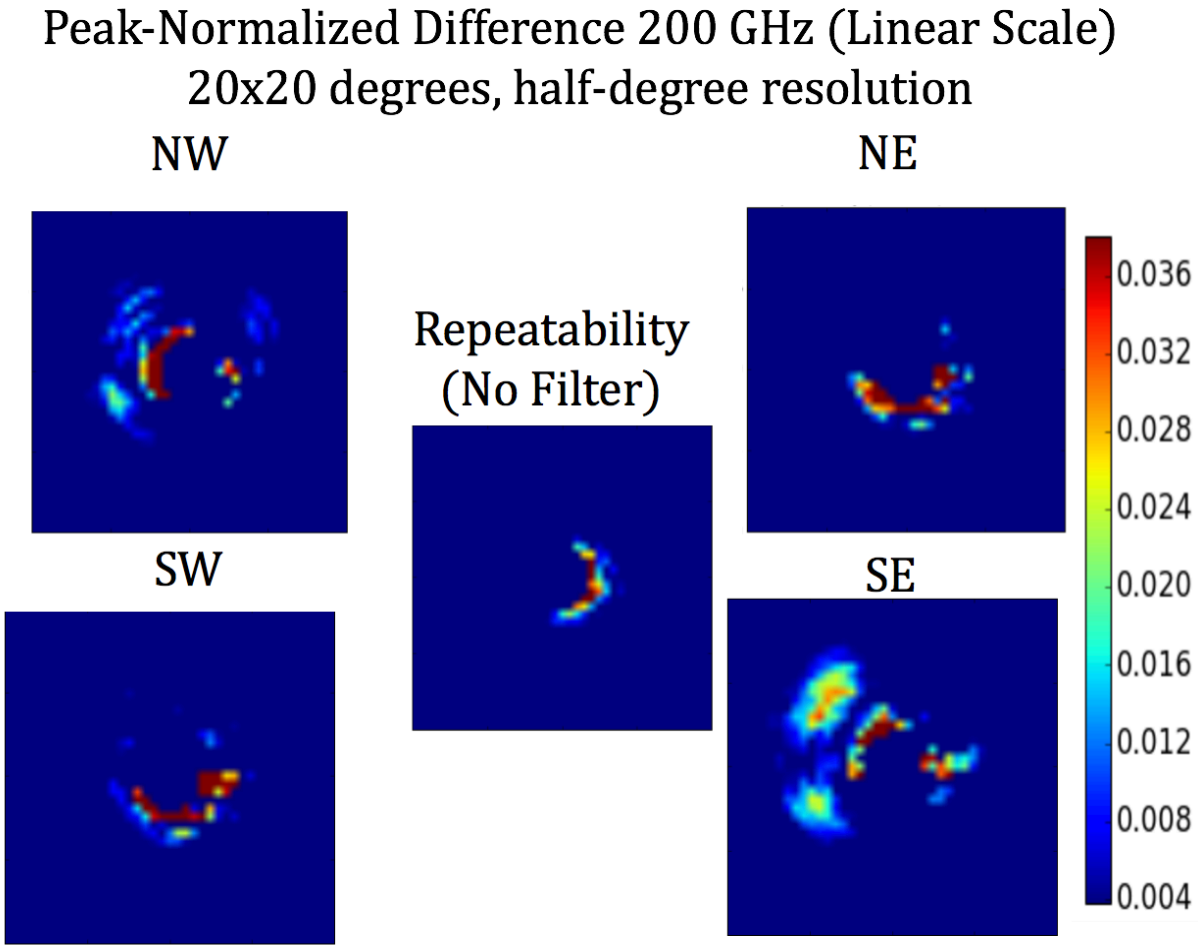

FIGURE 12. Peak-normalized difference plots of the amplitude of the Little Buddy diffraction pattern in linear scale. Measurements at all four quadrants (NW, NE, SE, SW), which are taken with the 1K low-pass filter, detect a higher amplitude modulation than the repeatability measurement taken without the filter. The SE quadrant contains the most dramatic amplitude modulation.

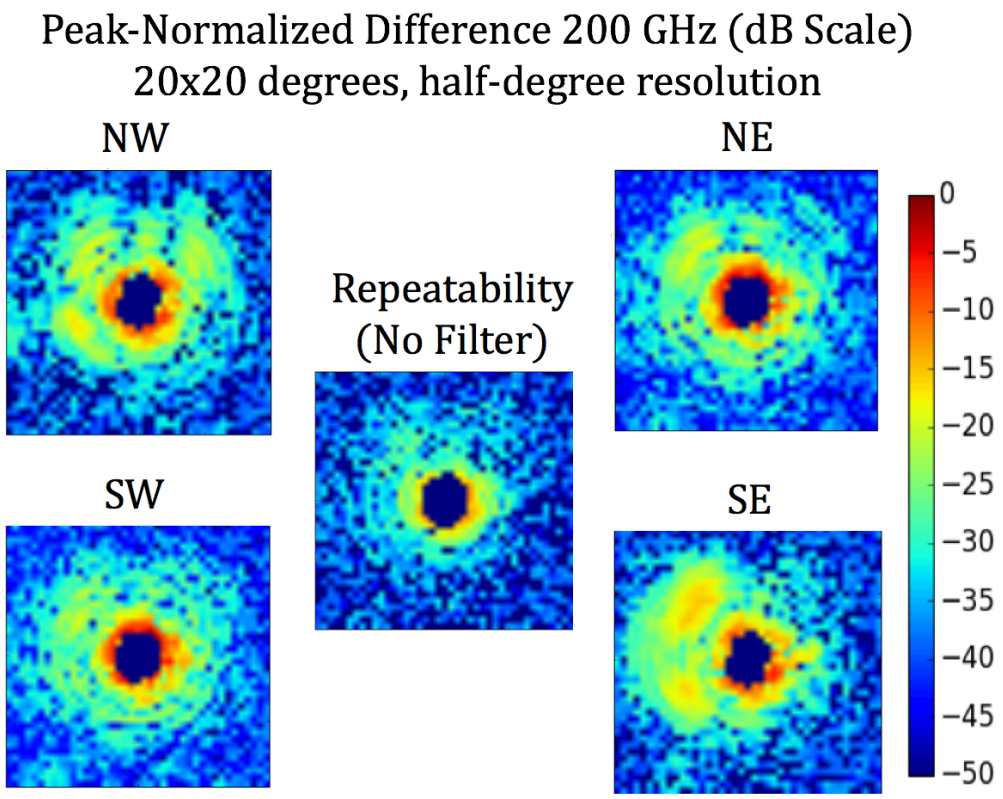

FIGURE 13. Peak-normalized difference plots of the amplitude of the Little Buddy diffraction pattern in dB scale. Measurements at all four quadrants (NW, NE, SE, SW), which are taken with the 1K low-pass filter, detect a higher amplitude modulation than the repeatability measurement taken without the filter. The SE quadrant contains the most dramatic amplitude modulation.

2.5 Analysis

Let us first analyze the repeatability (no-filter) measurement. Both the log and linear scale representations of this peak-normalized difference present clear evidence of crescent-shaped abnormality surrounding the center of the Gaussian beam. This suggests that (A) the beam coming out of the Tx horn was not completely Gaussian, (B) the Tx beam may or may not have been completely Gaussian, but the filter-lens-Rx horn system was misaligned such that the Rx-measured beam was not completely Gaussian, or (C), that some level of beam non-Gaussianity was caused by both the Tx and Rx sides of our experimental setup. Thankfully, we also needn't worry about these beam effects, for the little buddies we are trying to measure are located in a sidelobe further away from the beam (about 5 degrees in x and y away from the beam center). Thus, between any filter measurement and the repeatability measurement, all we must do is compare the amplitudes of the peak-normalized difference at any *particular* sidelobe point (where the little buddies should be located) rather than concern ourselves with the maximum amplitude of the peak-

normalized difference in the entire repeatability map.

Bearing this in mind, we see in Figures 12 and 13 that every spatial orientation of the filter has sidelobes about 5 degrees away from the beam center where the peak-normalized difference in amplitude modulation is greater than in the no-filter repeatability measurement. The most striking example of this is in the upper-left region of the SE map, where the peak difference is approximately -12.5 dB; this same region in the repeatability measurement has a peak difference of approximately -25db. Observing sidelobes in every spatial orientation of the filter, we conclude that the filter causes sidelobes which are not described by our repeatable model of a 2D Gaussian beam, suggesting that the filter modulates the amplitude of the 2D Gaussian beam produced by the Tx horn. Figures 12 and 13 measure this amplitude modulation, as received by the Rx horn.

3. Diffraction from a 2D Aperture

The above beam-mapping experiment supports, but does not prove, the hypothesis that the 1K low-pass filter of the MBAC is the source of Little Buddy diffraction. To prove that the Little Buddies are a diffraction pattern at all, we must measure the electric field of a source, such as a 2D Gaussian beam, both before and after it is modulated by the 1K filter, and compare these measurements. Electric field not only have an amplitude, which is measured by the experiment above, but a phase component. A brief overview of Fourier Optics will convince us that measuring both quantities, amplitude and phase, will be required if we are to determine whether or not the Little Buddies are a diffraction pattern. Suppose we have an input electric field, $E_0(x_0, y_0)$, propagating in the general +z direction from an input plane Σ_0. If Σ_0 diffracts E_0, then the resulting field, E(x, y; z), is [13]:

$$E(x,y;z) = -\frac{ik}{2\pi}\iint_{\Sigma_0} dx_0 dy_0 E_0(x_0,y_0)\frac{e^{ikr}}{r}$$

$$= -\frac{ik}{2\pi z}\iint_{\Sigma_0} dx_0 dy_0 E_0(x_0,y_0)\, e^{ik\sqrt{(x-x_o)^2+(y-y_0)^2+z^2}}$$

where we approximated $r \approx z$ in the denominator but not the exponential. The resulting integral is a convolution

$$E(x,y;z) = E_0 \odot S_H$$

with point-spread function (PSF) equal to [13]

$$S_H(x,y;z) = -\frac{ik}{2\pi z} e^{ik\sqrt{x^2+y^2+z^2}}$$

In our situation, E_0 is the electric field of the 2D Gaussian beam radiating from the millimeter-wave source, E is Little Buddy electric field, and we seek to find the PSF which corresponds to the Little Buddies. Using the convolution theorem,

$$F\{E_0\}F\{S_H\} = F\{E\}$$
$$S_H = F^{-1}\{F\{E\} / F\{E_0\}\}$$

Knowing the PSF, we have an exact mathematical model of the optical defect which is causing the Little Buddies. To get the PSF, we must know the amplitude and phase of both the pre-filter electric field (E) and post-filter diffraction pattern (E_0), which will require a system more sophisticated than that used in the 2D beam-mapping experiment above. We desire a system which can measure the amplitude *and* phase of the desired electric fields, and will call such a system "holographic imaging" system. This system ought to be capable of characterizing the spurious diffractions patterns (Little Buddies) caused by optical elements in the MBAC.

4. Holographic Imaging Techniques

The ultimate scientific goal of this project is to characterize, via holographic imaging techniques, optical elements or entire optical systems used by next-generation CMB experiments. The imaging techniques may be used to either diagnose unexpected behaviour of an optical system or to verify that the system works as expected.

4.1 Instrumentation

Figure 14 provides an overview of the holographic imaging system. Two voltage-controlled oscillators, LO 1 and LO 2, are controlled by separate phase-locked-loop (PLL) circuits. Each LO is programmed to output a single frequency between 10.5-13 GHz. The millimeter-wave source LO outputs f_1, and the LO distribution system is offset from f_1 by some MHz-range frequency, f_{OFFSET}. The millimeter-wave source is radiates onto an optical element you would like to test (DUT), and this optical element modulates the source signal in amplitude and/or phase. Both the reference (unmodulated) signal from the source and the modulated signal are received by Pacific Millimeter harmonic mixing systems (see "Reference Receiver" and "Modulated Receiver"); the offset LO signal is also passed to each mixer. Each harmonic mixing system acts as a frequency-domain multiplexer, discriminating an interference frequency (with frequency equal to Mf_{OFFSET}) from the input (source-frequency) signal and offset LO. The interference frequency or, "IF", of both the reference receiver and modulated receiver are correlated using a ROACH-2 FPGA board (or "ROACH"), which allows us to calculate the amplitude and phase of the modulation caused by the DUT. The receiver horn is electrically – isolated from the rest of the system, so as to avoid ground-loop effects with the millimeter-wave source.

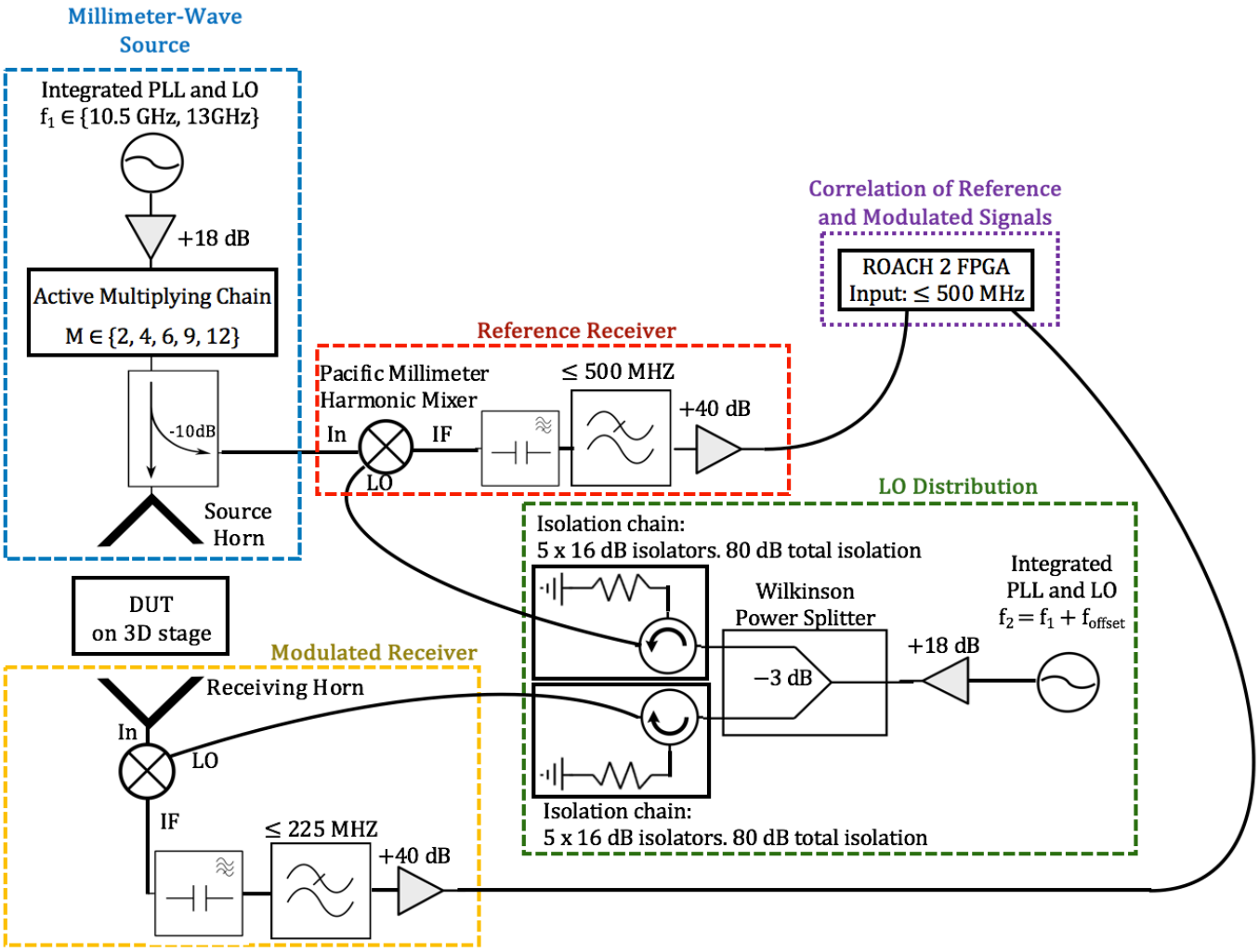

FIGURE 14. A system-level overview of the holographic imaging system. A millimeter-wave source feeds into a reference receiver and also radiates a signal which is modulated by an optical element that is being tested (DUT). The DUT sits atop a 3D rotational stage. Both the reference and modulated signals (pre and post DUT, respectively) are harmonically-mixed with an LO that is offset from the millimeter wave source by a frequency f_{OFFSET}. The harmonic mixing systems of each receiver act as a filter, discriminating an interference frequency caused by f_{OFFSET} and forcing this interference to travel away from the isolated LO distribution system. These interference frequencies are correlated using the ROACH-2 FPGA board.

4.1.1 Millimeter-Wave Source

An Analog Devices EV-ADF41020EB1Z evaluation board contains a voltage-controlled oscillator (VCO) in a phase-locked loop (PLL) and also contains an active-loop filtering system. The board also contains a 100 MHz temperature-compensated crystal oscillator (TCXO), which serves as a necessary reference signal to the PLL loop, and a USB interface which allows one to control the board's RF output. The evaluation board is used as a USB-controllable LO. The output of this LO is amplified by 18db and then sent through an active multiplying chain. The multiplying chain consists of a Norden Millimeter N08-1975 active frequency-doubler, and also a series of

Virginia Diodes passive frequency doublers and/or triplers. Based on the science requirements of any given use of the holographic imaging system, passive doublers and triplers are added such that the RF output of the LO may multiplied in frequency by a factor, M, equal to 2,4,6,9, or 12. The multiplied frequency is then sent through an integrated coupler and harmonic mixer. The mixed signal is sent to the reference receiver with a nominal coupling value of -10db. The other source signal radiates out of a waveguide whose dimensions must be chosen to match the millimeter-wave band chosen by the multiplicative factor M. The output frequency of the millimeter wave source is Mf_1.

4.1.2 LO Distribution System

An identical Analog Devices EV-ADF41020EB1Z evaluation board is used to produce an LO system with an output frequency of $f_2 = f_1 + f_{OFFSET}$, where f_{OFFSET} is typically of order tens of MHz. This output LO signal is then amplified by 18db and divided equally in power by a Wilkinson power splitter. Each of the two Wilkinson-split outputs are equal in power (half of the input power) and are of the same frequency as the LO, f_2. Each of these split signals is then sent through a chain of five 16 dB isolators. Thus, the total amount of isolation provided by each chain is 80dB. One of the isolated signals is sent to the reference receiver and the other is sent to the modulated receiver.

4.1.3 Reference and Modulated Receivers

The reference and modulated receivers behave exactly the same; the only difference between them is whether or not the input comes from the (unmodulated) millimeter-wave source or the (modulated) receiving horn. In both cases, the LO distribution signal of f_2 is mixed with a (modulated or unmodulated) signal with frequency Mf_1, producing an interference frequency at Mf_{OFFSET} (MHz). Due to the isolation chain, the IF is not allowed to travel back toward the LO distribution system, and so it is output from the mixer down a new line, which is input into the ROACH-2 correlator.

4.1.4 3D Beam Stage

The optical elements being tested (DUT) are placed at the origin of 3-axis rotational stage. This stage allows us to measure the DUT amplitude and phase modulation as a function of azimuth, elevation, and rotation. Each degree of freedom of the stage is powered by a Velmex 4800 Series rotary table. We rotate our Velmex stages at their maximum torque and minimum acceleration settings with a moderate (12.5-25 deg./s) angular velocity in order to minimize the shaking and vibration of our beam stage in between ROACH measurements.

4.1.5 The ROACH-2 Correlator

The ROACH-2 is a stand-alone field-programmable gate array (FPGA) board designed by the Collaboration for Astronomy Signal Processing and Electronics Research (CASPER). The ROACH-2 uses a Xilinx Virtex-6 SX475T FPGA and may be configured using a suite of proprietary "blocks" of Simulink code provided by both CASPER and Xilinx. A detailed list of ROACH-2 design features, as well as complete schematics for the ROACH-2 board, is published online by CASPER [14]. CASPER also publishes and routinely updates documentation on all of the Simulink blocks used to program the ROACH [15].

In our holography setup, the ROACH is configured as a wideband, 4-input correlator. There are four major components to the correlating system. First, each of the interference frequencies (IF), one from the modulated receiver and the other from the reference receiver, is sent to individual analog to digital converters (ADCs). Every clock cycle of the ROACH FPGA, the IF inputs are sampled and digitized into 8-bit binary point numbers in the range [-1, 1), and are then output by the ADC and sent to a Polyphase Filter Bank (PFB) Fast Fourier Transformer (FFT). The PFB technique helps avoid FFT leakage, which is the phenomenon where, depending on the sampling frequency and the number of points in the Fourier transform, an input tone (IF) appears in more than one output FFT frequency bin. The output of the PFB-FFT are four 36-bit complex values, where each of the complex values has an 18-bit real and 18-bit imaginary component. Each complex output corresponds to one of the ROACH correlator's four ADC inputs (however, we are only using two of these inputs, as we only have two IF signals). The PFB-FFT outputs then enter cross-multiplication engines, where the auto and cross-correlation of each IF signal is calculated. These correlated values are then accumulated in a ROACH memory register for a user-determined integration time. Once the integration time has passed, the accumulated, correlated values are averaged over the integration time and then saved in separate ROACH memory registers, read from the ROACH, and recorded as one holographic imaging "measurement".

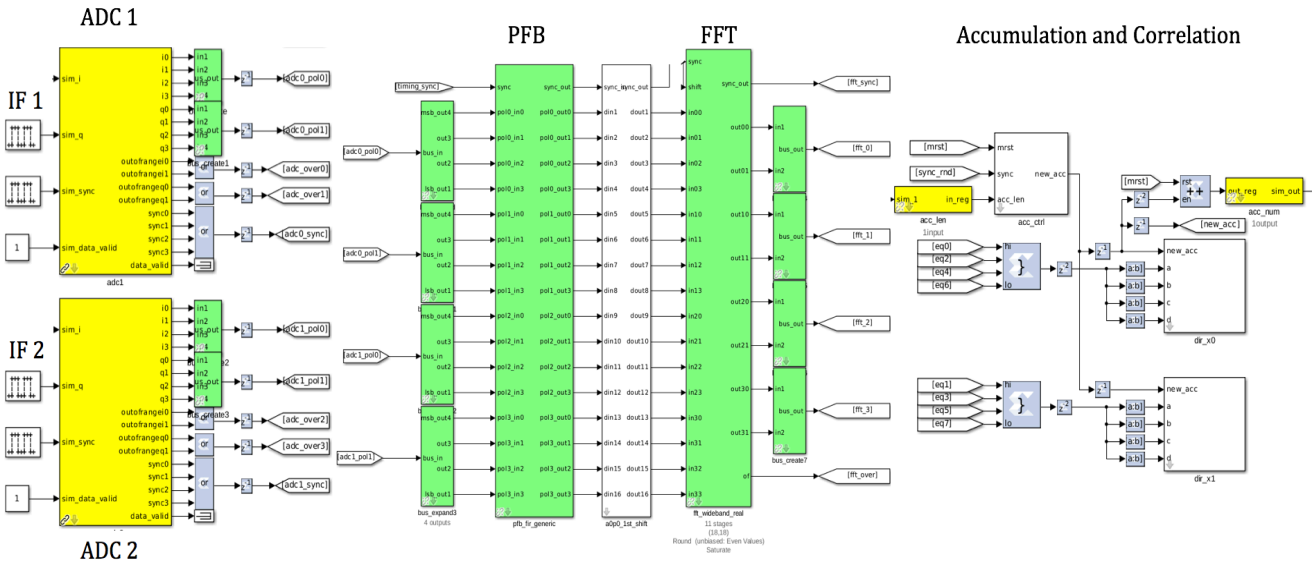

FIGURE 15. A screenshot of the Simulink block diagram used to program the ROACH-2 four-input correlator. Two interference frequencies, one from the reference receiver (IF 1) and one from the modulated receiver (IF 2), are sent to independent analog-to-digital converters (ADCs) and then Fast Fourier Transformed (FFT) using a Polyphase Filter Bank (PFB) technique to avoid channel-leakage. The auto and cross correlations of the IF signals are then calculated using cross-multiplication engines and then accumulated by the ROACH-2 for a user-determined integration time. The integrated (time-averaged) correlation signals are then allocated to memory on the ROACH-2 board; these allocated values are considered "measurements" of the holographic imaging system and are used to determine the amplitude and phase of the modulated DUT electric field.

We base our correlator-design on CASPER's standard wideband correlator tutorial [16]; all deviations from this design are described below. To begin, we clock both ROACH ADCs using a 500MHz not an 800MHz, source. This source frequency is important because it, along with the total number of (used or unused) correlator inputs, determines the Nyquist sampling frequency of our correlator. Since we program our ROACH to sample four inputs (yet only use two), the IFs we are correlating must not be greater than one quarter the clock frequency. Thus, using a 500 MHz clock, the IFs entering the ROACH correlator must not exceed 125 MHz.

The most significant design deviation we make from the CASPER model is that we remove the post-FTT 4-bit quantization architecture [16]. Thus, the 36-bit complex-valued outputs of the FFT, which are labelled 'fft_0', 'fft_1', 'fft_2', and 'fft_3' are *not* reduced in length to 4-bit real and 4-bit imaginary components. Instead, we pass *18-bit* real or imaginary components to the cross-multiplication engines ('dir_x1' and 'dir_x2') used to calculate the auto and cross correlations of our ROACH-2 inputs. Lastly, we change the overflow behavior of the FFT. Rather than 'wrapping' real or imaginary values that are too large to be represented by 18 bits during the FFT calculations, we allow

the extreme values, should they occur, to saturate any stage of the FFT. Removing the 4-bit quantization architecture and choosing saturated overflow behaviour ensures that the ROACH can detect DUT amplitude modulations with a 50dBm dynamic range.

4.1.6 Correlation: 50 dBm Dynamic Range

Understanding the ROACH's ability to correlate interference frequencies of different signals strengths is critically important to understanding the experimental limits of our holographic imaging system. We use the ROACH to correlate a reference-receiver IF signal with an IF that has been modulated in amplitude and phase by the optical element being testing (DUT). These measurements are recorded as a function of the three degrees of freedom of the beam stage: azimuth, elevation, and rotation. Thus, both the DUT and the beam stage uniquely affect the strength of the modulated receiver signal. Care must be taken to ensure that the ROACH *can*, indeed, correlate the modulated IF with the reference IF despite these significant changes in modulated IF signal-strength. To do this, one must ensure that every stage of the ROACH programming (such as the ADCs, PFB-FFT, cross-multiplication engines, and accumulator) allocates enough memory to meaningfully calculate complex values whose magnitudes vary by several orders of magnitude. At the same time, the ROACH board does not have infinite RAM or processing capabilities. Considering the design constraints of the ROACH-2, we follow CASPER in storing ADC outputs as 8-bit binary-point values, and allow these numbers to expand to 18-bits for both the real and imaginary outputs of the PFB-FFT. This 18-bit quantization, as opposed to 4-bit quantization done in the CASPER model, is sufficient to represent most signals entering the ROACH during our holographic measurements. If ever one of the IF signal strengths is so large that its complex Fourier-transformed value cannot be represented by 36 bits (18 real and 18 imaginary), then we choose to *saturate* the FFT value rather than wrap the overflow value. Saturation overflow behaviour allows us to ensure that the FFT is always comparing ROACH signals at some "baseline" power level, regardless of what the baseline is. One cannot meaningfully compare the amplitude and phase of IF signals in different ROACH measurements if the FFT wraps during any stage of data accumulation between measurements. By electing 18-bit, rather than 4-bit quantization after the PFB-FFT, while also saturating (rather than wrapping) FFT overflow behaviour, our ROACH can correlate interference frequencies that differ in power up to 50dBm.

By adjusting the ROACH integration time, as well as the power of the millimeter-wave source, one can select the specific 50dBm

range of power values which can be measured by the ROACH. The integration time is controlled by the CASPER-SIMULINK "acc_cntrl" block [17]. One may adjust the power of the millimeter-wave source by either attenuating the LO output (before the +18dB amplifier) or by inserting microwave-absorbing material, such as Eccosorb, into the source horn. We have tested our millimeter-wave source in the range –(10-28)dBm, and then adjusted the integration time accordingly so that we could detect modulated amplitude features at –(60-78) dBm, respectively.

4.2 Results – AdvACT LF Horn Array

Due to Advanced ACTPol (AdvACT) testing schedules, it has not yet been possible to use the holographic imaging system to measure amplitude and phase modulations caused by the MBAC 1K low-pass filter. Rather, priority was placed on testing one of the AdvACT low frequency (LF) feed horn arrays. AdvACT is an upgrade to the ACTPol polarimeter, designed to observe CMB polarization across five different frequency bands (27-230 GHz) [18]. This wide frequency coverage and fine angular resolution (1.4′ at 150 GHz) of AdvACT will significantly improve existing constraints on dark energy, the sum of the neutrino masses, and the existence of primordial gravitational waves [19]. AdvACT uses the same off-axis Gregorian telescope as the ACT, whose optical chain consists of a 6m diameter primary mirror, a 2m diameter secondary mirror and a set of three optics tubes. Each tube consists of a window, filter stack, three silicon reimaging optics, a feedhorn array and finally the detector focal plane.

The AdvACT upgrade has already replaced each of ACTPol's three detector arrays, replacing optics tube elements to accommodate different frequency bands. The 2017 season configuration consists of one high frequency (HF) array, observing at 230 and 150 GHz, and two mid-frequency (MF) arrays, observing at 150 and 90 GHz [19]. The LF detector array is the last component of AdvACT to be deployed, which will replace one of the MF arrays and observe at frequencies centered at 27 and 39 GHz [18]. Single-frequency observations of the CMB are limited by foregrounds such as synchrotron emission, spinning dust emission, galactic dust, and DSFG's. AdvACT's high and low frequency coverage allows for the removal of these foregrounds; the LF array helps remove synchrotron and spinning dust emission.

Below are preliminary results of the high-frequency limit of the AdvACT LF Feed Horn Array centered at 39 GHz. The E-plane, H-plane, and cross-polarization measurements taken with the holographic imaging system are compared to electromagnetic simulations which were calculated using High Frequency Structure Simulator (HFSS) software.

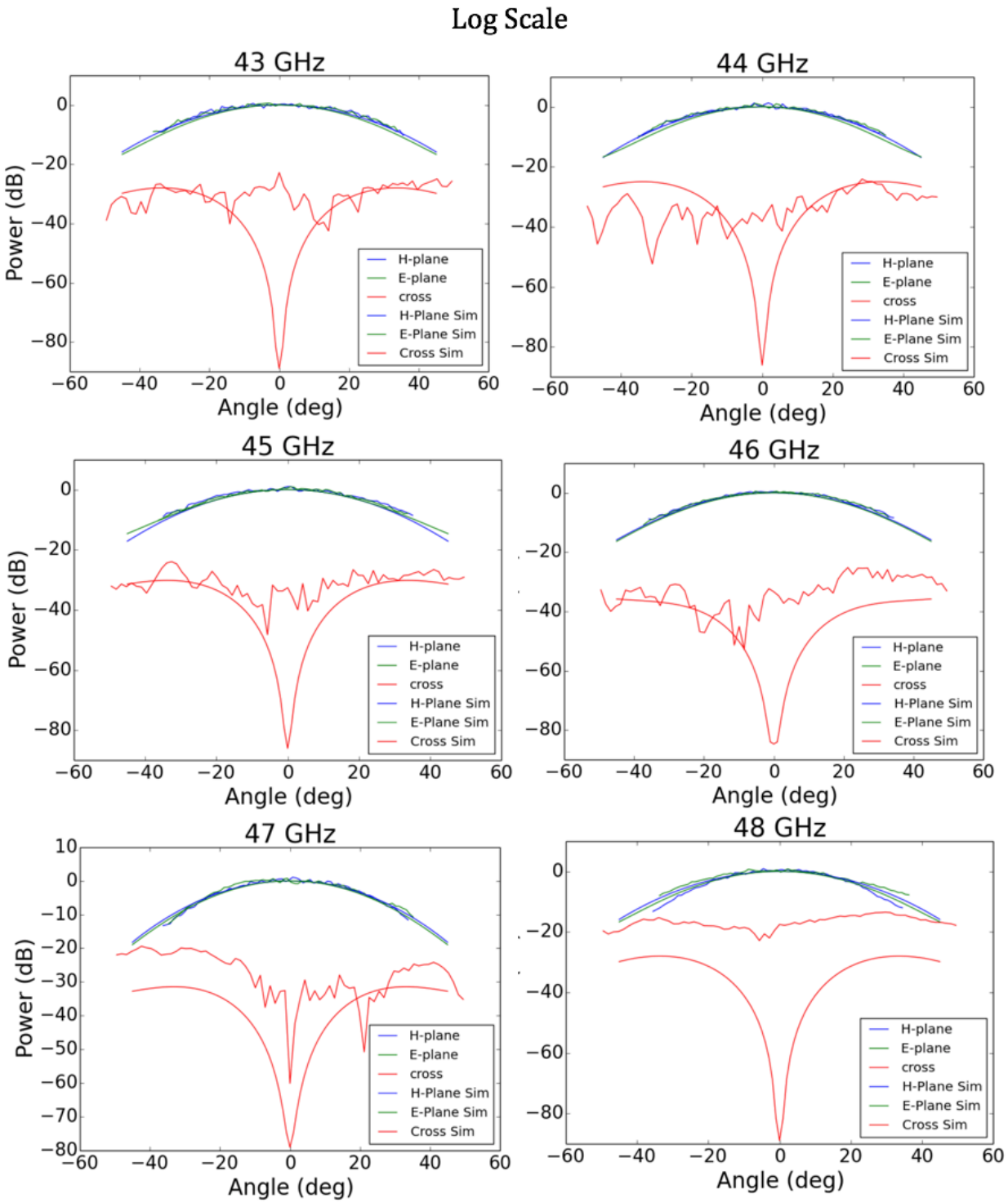

FIGURE 16. E and H-plane cuts of the AdvACT LF array, are plotted in log scale as a function of angle. The cuts are also compared to their predicted values, which are calculated using an HFSS simulation. Cross-polarization leakage is also plotted. The measured and simulated beam widths agree to within tolerances that merit deploying the LF array to the ACT in Chile.

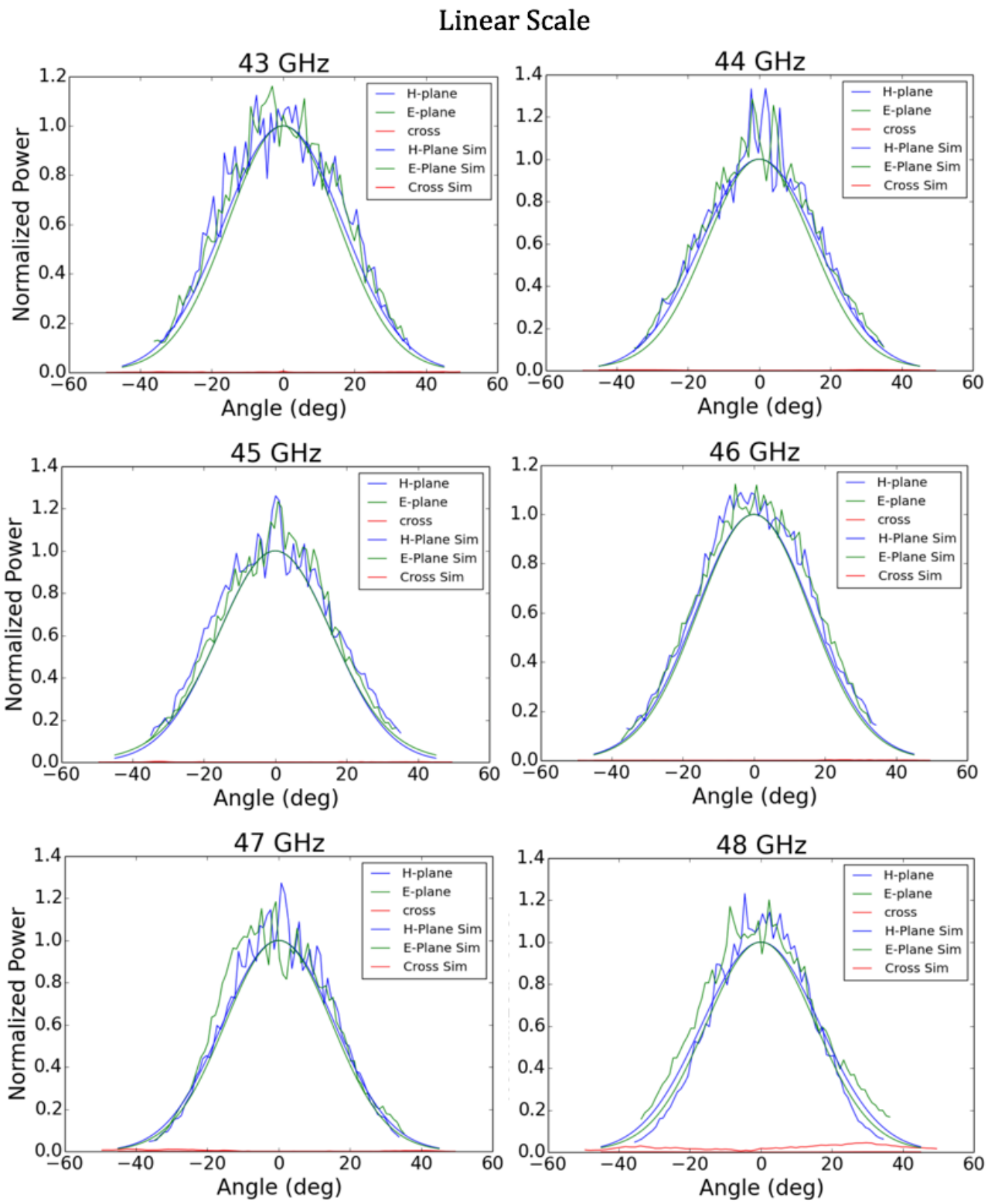

FIGURE 17. E and H-plane cuts of the AdvACT LF array, are plotted in linear scale as a function of angle. The cuts are also compared to their predicted values, which are calculated using an HFSS simulation. Cross-polarization leakage is also plotted. The measured and simulated beam widths agree to within tolerances that merit deploying the LF array to the ACT in Chile.

4.3 Analysis

Figures 16 and 17 demonstrate that the beam shape (in E and H cuts) of the LF feed horn array matches agree with simulation from 43-48 GHz. Further, the cross-polarization leakage of the feed-horn array is always (at least) -17dB below the peak beam strength, which is sufficient for deploying the LF array to the ACT in Chile.

For each frequency measurement, at the maximum beam strength (angle = 0 deg.), the dynamic range in power of the holography measurements is between, approximately, -60dBm and -17 dBm. The precise reason that this dynamic range differs from the expected value of 50dB is still being determined, but one significant factor for this deviation is power fluctuations in the millimeter-wave source. Over the course of a fixed-frequency H-plane or E-plane measurement, which currently takes ~10 minutes to complete, the millimeter-wave source drifts in power by greater than 3dB. There are currently two possible explanations for this fluctuation (though, we cannot discount the fact that currently-unknown phenomena may be causing a significant amount of this fluctuation). First, stray reflections from the laboratory environment may be entering the millimeter-wave source. To circumvent this, an isolating chain could be placed on the source's LO output. Alternatively, a study is underway to see if the power fluctuations correlate with certain angular positions of the beam stage in our laboratory environment; identifying such a correlation would allow us to eliminate or avoid these stray environmental reflections when recording measurements with the holographic imaging system. The second potential cause of the power fluctuation may be that the 18 dB amplifier in the millimeter-wave source injects a signal that is too-powerful into the active multiplying chain system. Care will have to be taken when studying the source fluctuation as a function of mean LO power output, so as to not introduce new systematic effects when attenuating the LO. Possible, new systematic effects may be introduced by using in-line SMA attenuators or other imperfect attenuators.

5. Conclusion

An historical account of the cosmic microwave background (CMB) has been discussed, which motivates the study of temperature anisotropies in the CMB and their implications for the homogeneity and isotropy of the universe, as well as the formation of structure in the early universe. Current studies of CMB anisotropy require diffraction-limited optical systems; achieving this level of sensitivity requires a thorough understanding of the diffraction patterns caused by all optically-active components in an instrument. Little Buddies, an unexpected diffraction pattern found in the ACT's MBAC receiver, are

studied by measuring the amplitude of modulations caused by the 1K-low pass filter in the 215 GHz array of the MBAC. A discussion of Fourier optics is presented to determine the relation between amplitude (and phase) modulations by 2D optical elements (such as the 1K filter) and their far-field diffraction patterns (e.g. Little Buddies). A holographic imaging system is being developed which can measure both the amplitude and phase of modulations caused by optically-active components and systems. We present preliminary beam mapping measurements made using the holographic system, comparing the system's current sensitivity with its expected 50 dBm dynamic range. The holographic system is used to measure the beam shape and cross-polarization leakage of a next-generation, Advanced ACTPol feed horn array. These measurements merit the feed horn array's deployment to the ACT in Chile. Even though the holographic imaging system has not yet sustained an expected dynamic range of 50dBm during DUT measurements, it has still meaningfully contributed to the commissioning of next-generation CMB instrumentation.

6. Acknowledgements

I wish to thank my advisor, Jeff McMahon, for four years of mentorship that has thoroughly prepared me for advanced study in cosmology. Jeff is a man of great energy and humility, and these qualities are reflected in his work with students. Jeff's supremely-earnest work ethic demonstrated to me that there is beauty in understanding fundamental natural phenomena; his demonstration is why I chose to study physics at University.

I am indebted to Jean Krisch, for enabling me to seize fulfilling professional opportunities that accorded with my academic pursuits. She has shown me what it means to be a forthright and formidable mentor. I wish her the best in her retirement.

Thank you to Jacob Curtis, Alexander Kavner, and Shubhankhar Sahai for demonstrating to me what merits and achievements and undergraduate may achieve, so long as they adopt the right disposition. To Dave and Tommy for teaching me what it means to be collegiate and what it means to be trivial.

Thank you to my mother, to whom everything is dedicated. To Grandma Elly, to Grandpa Don, to my father. To Aaron, my best friend and mooring post.

7. References

[1] Ryden, Barbara S. Introduction to Cosmology. 1st ed. San Francisco: Addison Wesley, 2003. Print.

[2] Kolb, Edward W., and Michael S. Turner. The Early Universe. N.p: Westview Press, pp. 8-9, 1990.

[3] Dicke, R. H., et. al. Astrophysical Journal, vol. 142, p.414-419

[4] Penzias, A. A. and Wilkinson, R. W. Astrophysical Journal, vol. 142, p.419-421

[5] Arfken, G. Mathematical Methods for Physicists, 3rd ed. Orlando, FL: Academic Press, 1985

[6] Read, David D. "Acoustic Peaks and the Cosmological Parameters." Level 5 Knowledgebase for Extragalactic Astronomy and Cosmology. CalTech, Pasadena. Lecture. Link: https://ned.ipac.caltech.edu/level5/Sept0/Reid/Reid5_2.html

[7] Hlozek, Renee, and Jeff J. McMahon. "CMB Data Analysis Summer School." University of Michigan, Ann Arbor. Aug. 2016. Code Repository:https://github.com/jeffmcm177/CMBAnalysis_SummerSchool

[8] ACT Collaboration. “ACT Data Products at LAMBDA.” LAMBDA - Data Products, NASA GSFC,lambda.gsfc.nasa.gov/product/act/act_prod_table.cfm.

[9] Filippini, J.P., *et. al.* arXiv:1106.2158 [astro-ph.CO]

[10] Plank Collaboration. arXiv:1303.5067 [astro-ph.CO]

[11] R. J. Thornton et al., ApJS 227, 21 (2016)

[12] arxiv.org/abs/1007.0290v1

[13] Kim, Myung K. “Chapter 2. Diffraction and Fourier Optics.” Digital Holographic Microscopy: Principles, Techniques, and Applications, Springer, 2011.

[14] “ROACH-2 Revision 2.” CASPER, Collaboration for Astronomy Signal Processing and Electronics Research, casper.berkeley.edu/wiki/ROACH-2_Revision_2.

[15] "Libraries". CASPER, Collaboration for Astronomy Signal Processing and Electronics Research, https://casper.berkeley.edu/ wiki/ Libraries

[16] " Tutorial Wideband Pocket Correlator", CASPER, Collaboration for Astronomy Signal Processing and Electronics Research,https://casper.berkeley.edu/wiki/Tutorial_Wideband_Pocket_Correlator

[17] " Wideband Spectrometer", CASPER, Collaboration for Astronomy Signal Processing and Electronics Research, https://casper.berkeley.edu/wiki/Tutorials#Wideband_Spectrometer

[18] Koopman, B., Cothard, N. F., Choi, S. K., et al. Advanced ACTPol Low Frequency Array: Readout and Characterization of Prototype 27 and 39 GHz Transition Edge Sensors, Journal of Low Temperature Physics (November 7, 2017);arXiv: 1711.02594.

[19] S. W. Henderson et al., Journal of Low Temperature Physics 184, 3, 772 (2016), ISSN1573-7357, doi:10.1007/s10909-016-1575-z.